Sciencexpress Reports

# Chirality density wave of the "hidden order" phase in $URu_2Si_2$

**H.-H. Kung,[1*] R. E. Baumbach,[2†] E. D. Bauer,[2] V. K. Thorsmølle,[1‡] W.-L. Zhang,[1] K. Haule,[1*] J. A. Mydosh,[3] G. Blumberg[1,4*]**

[1]Department of Physics and Astronomy, Rutgers University, Piscataway, New Jersey 08854, USA. [2]Los Alamos National Laboratory, Los Alamos, New Mexico 87545, USA. [3]Kamerlingh Onnes Laboratory, Leiden University, 2300 RA Leiden, Netherlands. [4]National Institute of Chemical Physics and Biophysics, 12618 Tallinn, Estonia.

*Corresponding author. E-mail: girsh@physics.rutgers.edu (G.B.); haule@physics.rutgers.edu (K.H.); skung@physics.rutgers.edu (H.-H.K.)

†Present address: National High Magnetic Field Laboratory, Florida State University, Tallahassee, FL 32310, USA.

‡Present address: Department of Physics, University of California, San Diego, La Jolla, CA 92093, USA, and Department of Physics, Boston University, Boston, MA 02215, USA.

**A second-order phase transition in a physical system is associated with the emergence of an "order parameter" and a spontaneous symmetry breaking. The heavy fermion superconductor $URu_2Si_2$ has a "hidden order" (HO) phase below the temperature of 17.5 K; the symmetry of the associated order parameter has remained ambiguous. Here we use polarization resolved Raman spectroscopy to specify the symmetry of the low energy excitations above and below the HO transition. We determine that the HO parameter breaks local vertical and diagonal reflection symmetries at the uranium sites, resulting in crystal field states with distinct chiral properties, which order to a commensurate chirality density wave ground state.**

In solids, electrons occupying 5*f* orbitals often have a partly itinerant and partly localized character, which leads to a rich variety of low temperature phases, such as magnetism and superconductivity (*1*). Generally, these ordered states are characterized by the symmetry they break, and an order parameter may be constructed to describe the state with reduced symmetry. In a solid, the order parameter reflects the microscopic interactions among electrons that lead to the phase transition. In materials containing *f*-electrons, exchange interactions of the lanthanide or actinide magnetic moments typically generate long-range antiferromagnetic or ferromagnetic order at low temperatures, but multipolar ordering such as quadrupolar, octupolar and hexadecapolar is also possible (*2*).

One particularly interesting example is the uranium-based inter-metallic compound $URu_2Si_2$. It displays a non-magnetic second-order phase transition into an electronically ordered state at $T_{HO} = 17.5$ K, and then becomes superconducting below 1.5 K (*3*, *4*). Despite numerous theoretical proposals to explain the properties below $T_{HO}$ in the past 30 years (*5*–*10*), the symmetry and microscopic mechanism for the order parameter remain ambiguous, hence the term "hidden order" (HO) (*11*). In this ordered state, an energy gap in both the spin and the charge response have been reported (*12*–*18*). In addition, an in-gap collective excitation at a commensurate wave vector has been observed in neutron scattering experiments (*13*, *14*, *16*). Recently, four-fold rotational symmetry breaking under an in-plane magnetic field (*19*) and a lattice distortion along the crystallographic *a*-axis (*20*) have been reported in high quality small crystals. However, the available experimental works can not yet conclusively determine the symmetry of the order parameter in the HO phase.

$URu_2Si_2$ crystallizes in a body-centered tetragonal structure belonging to the $\mathbb{D}_{4h}$ point group (space group No. 139 *I*4/*mmm*, Fig. 1A). The uniqueness of $URu_2Si_2$ is rooted in the coexistence of the broad conduction bands, comprised mostly of Si-*p* and Ru-*d* electronic states, and more localized U-5*f* orbitals, which are in a mixed valent configuration between tetravalent $5f^2$ and trivalent $5f^3$ (*21*). When the temperature is lowered below approximately 70 K, the hybridization with the conduction band allows a small fraction of each U-5*f* electron to participate in formation of a narrow quasiparticle band at the Fermi level, whereas the rest of the electron remains better described as localized on the uranium site.

In the dominant atomic configuration, the orbital angular momentum and spin of the two quasi-localized U-5*f* electrons add up to total momentum $4\hbar$, having nine-fold degeneracy (*6*, *22*). In the crystal environment of $URu_2Si_2$, these states split into seven energy levels denoted by irreducible representations of the $\mathbb{D}_{4h}$ group: 5 singlet states $2A_{1g} \oplus A_{2g} \oplus B_{1g} \oplus B_{2g}$ and 2 doublet states $2E_g$. Each irreducible representation possesses distinct symmetry properties under operations such as reflection, inversion, and rotation. For example, the $A_{1g}$ states are invariant under all symmetry operations of the $\mathbb{D}_{4h}$ group, whereas the $A_{2g}$ state changes sign under all diagonal and vertical reflections, and thereby has 8 nodes (Fig. 1A). Most of the physical observables, such as density-density and stress tensors, or one particle spectral functions, are symmetric under exchange of *x*- and *y*-axis in tetragonal structure and therefore are impervious to the $A_{2g}$ excitations, whereas these $A_{2g}$ excitations can be probed by Raman spectroscopy (*23*–*28*).

Raman scattering is an inelastic process which promotes

excitations of controlled symmetry defined by the scattering geometries, namely polarizations of the incident and scattered light (*22*, *23*). Polarization resolved Raman spectroscopy enables separation of the spectra of excitations into distinct symmetry representations, such as $A_{1g}$, $A_{2g}$, $B_{1g}$, $B_{2g}$ and $E_g$ in the $\mathbb{D}_{4h}$ group thereby classifying the symmetry of the collective excitations (*22*, *26*). The temperature evolution of these excitations across a phase transition provides an unambiguous identification of the broken symmetries; furthermore, the photon field used by Raman probe is weak, which avoids introducing external symmetry breaking perturbations.

We employ linearly and circularly polarized light to acquire the temperature evolution of the Raman response functions in all symmetry channels. In Fig. 2 we plot the Raman susceptibility in the $A_{2g}$ channel, where the most significant temperature dependence was observed. The Raman susceptibility above $T_{HO}$ can be described within a low energy minimal model suggested in Ref. (*6*) (illustrated in Fig. 1B) that contains two singlet states of $A_{2g}$ and $A_{1g}$ symmetries, split by an energy $\omega_0$, and a conduction band of predominantly $A_{1g}$ symmetry. In the following, we denote the singlet states of $A_{2g}$ and $A_{1g}$ symmetries by $|\mathbb{0}\rangle$ and $|\mathbb{1}\rangle$; the conduction band is labeled $|CB\rangle$.

At high temperatures, the Raman spectra exhibits a Drude-like line shape, which in Ref. (*25*) was attributed to quasi-elastic scattering. The maximum in the Raman response function decreases from 5 meV at room temperature to 1 meV just above $T_{HO}$ (Fig. 2A). Below 70 K, the line shape deviates slightly from the Drude function, tracking the formation of the heavy fermion states by the hybridization of the itinerant conduction band and the U-5*f* states. Below 17.5 K, the $A_{2g}$ Raman response function shows suppression of low energy spectral weight resembling the temperature dependence of BCS gap function, and the emergence of a sharp in-gap mode at 1.6 meV (Fig. 2, A and C).

Figure 2B displays a comparison between the static Raman susceptibility $\chi'_{A_{2g}}(0,T)$ (left axis) and the *c*-axis static magnetic susceptibility $\chi_c^m(T)$ (right axis), showing that the responses are proportional to each other at temperatures above $T_{HO}$. This proportionality can be understood by noting that both susceptibilities probe $A_{2g}$-like excitations as given by the minimal model of Fig. 1B. The extreme anisotropy of the magnetic susceptibility (Fig. 2B) also follows from this minimal model (*22*).

Having established the Raman response of $A_{2g}$ symmetry and its correspondence with the magnetic susceptibility, we now present our main results describing the symmetry breaking in the HO state. Figure 3 shows the Raman response in six scattering geometries at 7 K. The intense in-gap mode is observed in all scattering geometries containing $A_{2g}$ symmetry. The mode can be interpreted as a $\omega_0 = 1.6$ meV resonance between the $|\mathbb{0}\rangle$ and $|\mathbb{1}\rangle$ quasi-localized states, which can only appear in the $A_{2g}$ channel of the $\mathbb{D}_{4h}$ group. A weaker intensity is also observed at the same energy in XX and $X'X'$ geometries commonly containing the excitations of the $A_{1g}$ symmetry, and a much weaker intensity is barely seen within the experimental uncertainty in RL geometry.

The observation of this intensity "leakage" into forbidden scattering geometries marks the lowering of symmetry in the HO phase, indicating the reduction of the number of irreducible representations of the parent point group, $\mathbb{D}_{4h}$. For example, the $\omega_0$ mode intensity "leakage" from the $A_{2g}$ into the $A_{1g}$ channel implies that the irreducible representation $A_{1g}$ and $A_{2g}$ of the $\mathbb{D}_{4h}$ point group merge into the $A_g$ representation of the lower group $\mathbb{C}_{4h}$. This signifies the removal of the local vertical and diagonal reflection symmetry operators at the uranium sites in the HO phase. Similarly, the tiny intensity leakage into the RL scattering geometry measures the strength of orthorhombic distortion caused by broken four-fold rotational symmetry.

When the reflection symmetries are broken, an $A_{2g}$-like interaction operator $\Psi_{HO} \equiv V|\mathbb{1}\rangle\langle\mathbb{0}|$ mixes the $|\mathbb{0}\rangle$ and $|\mathbb{1}\rangle$ states leading to two new local states:

$$|\aleph^+\rangle \approx (1-\frac{V^2}{2\omega_0^2})|\mathbb{0}\rangle + \frac{V}{\omega_0}|\mathbb{1}\rangle \quad (1)$$

$$|\aleph^-\rangle \approx (1-\frac{V^2}{2\omega_0^2})|\mathbb{0}\rangle - \frac{V}{\omega_0}|\mathbb{1}\rangle \quad (2)$$

with $V$ being the interaction strength (*6*). A pair of such states cannot be transformed into one another by any remaining $\mathbb{C}_{4h}$ group operators: a property known as chirality (or handedness). The choice of either the right-handed or the left-handed state on a given uranium site, $|\aleph^+\rangle$ or $|\aleph^-\rangle$, defines the local chirality in the HO phase (Fig. 1C). Notice that these two degenerate states both preserve the time reversal symmetry, carry no spin and contain the same charge, but differ only in handedness.

The same 1.6 meV sharp resonance has also been observed by inelastic neutron scattering at momentum commensurate with the reciprocal lattice vector, but only in the HO state (*14*, *16*, *29*). The Raman measurement proves that this resonance is a long-wavelength excitation of the $A_{2g}$ character. The appearance of the same resonance in the neutron scattering at a different wavelength, corresponding to the *c*-axis lattice constant, requires HO to be a staggered alternating electronic order in *c* direction. Such order with alternating left and right handed states at the uranium sites

for neighboring basal planes has no modulation of charge or spin, and does not couple to tetragonal lattice, hence it is hidden to all probes but the scattering of $A_{2g}$ symmetry. We reveal this hidden order to be a chirality density wave depicted in Fig. 1D.

The chirality density wave doubles the translational periodicity of the phase above $T_{HO}$, hence it folds the electronic Brillouin zone, as recently observed by angle-resolved photoemission spectroscopy (*30*). It also gives rise to an energy gap, as previously observed in optics (*12*, *17*, *18*) and tunneling experiments (*15*, *31*), and shown in Fig. 2C to originate in expelling the continuum of $A_{2g}$ excitations. The sharp resonance is explained by excitation from the ground state, in which a chirality density wave staggers $|\aleph^{+}\rangle$ and $|\aleph^{-}\rangle$, to the excited collective state (*22*).

A local order parameter of primary $A_{2g}$ symmetry, breaking vertical/diagonal reflections, with subdominant $B_{1g}$ component, breaking four-fold rotational symmetry, can be expressed in terms of the composite hexadecapole local order parameter of the form (*6*, *22*):

$$\pm V\overline{(J_x - J_y)(J_x + J_y)(J_x J_y + J_y J_x)} \qquad (3)$$

where $J_x$, $J_y$ are in-plane angular momentum operators and the overline stands for symmetrization. A spatial order alternating the sign of this hexadecapole for neighboring basal planes is the chirality density wave (Fig. 1D) that consistently explains the HO phenomena as it is observed by Raman and neutron scattering (*13*, *14*, *16*, *29*), magnetic torque (*19*), X-ray diffraction (*20*), and other data (*11*, *12*, *17*, *18*, *30*). Our finding is an example of exotic electronic ordering emerging from strong interaction among *f* electrons, which should be a more generic phenomenon relevant to other intermetallic compounds.

*Note added in proof*: While this paper was being reviewed, J. Buhot *et al.* (*32*) reproduced the $A_{2g}$ symmetry in-gap mode in a Raman experiment with 561 nm laser excitation and showed that the mode does not split in up to 10 T magnetic field.

## REFERENCES AND NOTES


1. G. R. Stewart, Heavy-fermion systems. *Rev. Mod. Phys.* **56**, 755–787 (1984). doi:10.1103/RevModPhys.56.755
2. P. Santini, S. Carretta, G. Amoretti, R. Caciuffo, N. Magnani, G. Lander, Multipolar interactions in f-electron systems: The paradigm of actinide dioxides. *Rev. Mod. Phys.* **81**, 807–863 (2009). doi:10.1103/RevModPhys.81.807
3. T. T. M. Palstra, A. A. Menovsky, J. van den Berg, A. J. Dirkmaat, P. H. Kes, G. J. Nieuwenhuys, J. A. Mydosh, Superconducting and magnetic transitions in the heavy-fermion system $URu_2Si_2$. *Phys. Rev. Lett.* **55**, 2727–2730 (1985). Medline doi:10.1103/PhysRevLett.55.2727
4. M. B. Maple, J. W. Chen, Y. Dalichaouch, T. Kohara, C. Rossel, M. S. Torikachvili, M. W. McElfresh, J. D. Thompson, Partially gapped Fermi surface in the heavy-electron superconductor $URu_2Si_2$. *Phys. Rev. Lett.* **56**, 185–188 (1986). Medline doi:10.1103/PhysRevLett.56.185
5. P. Santini, G. Amoretti, Crystal field model of the magnetic properties of $URu_2Si_2$. *Phys. Rev. Lett.* **73**, 1027–1030 (1994). Medline doi:10.1103/PhysRevLett.73.1027
6. K. Haule, G. Kotliar, Arrested Kondo effect and hidden order in $URu_2Si_2$. *Nat. Phys.* **5**, 796–799 (2009). doi:10.1038/nphys1392
7. S. Elgazzar, J. Rusz, M. Amft, P. M. Oppeneer, J. A. Mydosh, Hidden order in $URu_2Si_2$ originates from Fermi surface gapping induced by dynamic symmetry breaking. *Nat. Mater.* **8**, 337–341 (2009). Medline doi:10.1038/nmat2395
8. P. Chandra, P. Coleman, J. A. Mydosh, V. Tripathi, Hidden orbital order in the heavy fermion metal $URu_2Si_2$. *Nature* **417**, 831–834 (2002). Medline doi:10.1038/nature00795
9. H. Ikeda, M.-T. Suzuki, R. Arita, T. Takimoto, T. Shibauchi, Y. Matsuda, Emergent rank-5 nematic order in $URu_2Si_2$. *Nat. Phys.* **8**, 528–533 (2012). doi:10.1038/nphys2330
10. P. Chandra, P. Coleman, R. Flint, Hastatic order in the heavy-fermion compound $URu_2Si_2$. *Nature* **493**, 621–626 (2013). Medline doi:10.1038/nature11820
11. J. A. Mydosh, P. M. Oppeneer, Colloquium: Hidden order, superconductivity, and magnetism: The unsolved case of $URu_2Si_2$. *Rev. Mod. Phys.* **83**, 1301–1322 (2011) and references therein. doi:10.1103/RevModPhys.83.1301
12. D. A. Bonn, J. D. Garrett, T. Timusk, Far-infrared properties of $URu_2Si_2$. *Phys. Rev. Lett.* **61**, 1305–1308 (1988). Medline doi:10.1103/PhysRevLett.61.1305
13. C. Broholm, H. Lin, P. Matthews, T. Mason, W. Buyers, M. Collins, A. Menovsky, J. Mydosh, J. Kjems, Magnetic excitations in the heavy-fermion superconductor $URu_2Si_2$. *Phys. Rev. B* **43**, 12809–12822 (1991). doi:10.1103/PhysRevB.43.12809
14. C. R. Wiebe, J. A. Janik, G. J. MacDougall, G. M. Luke, J. D. Garrett, H. D. Zhou, Y.-J. Jo, L. Balicas, Y. Qiu, J. R. D. Copley, Z. Yamani, W. J. L. Buyers, Gapped itinerant spin excitations account for missing entropy in the hidden-order state of $URu_2Si_2$. *Nat. Phys.* **3**, 96–99 (2007). doi:10.1038/nphys522
15. P. Aynajian, E. H. da Silva Neto, C. V. Parker, Y. Huang, A. Pasupathy, J. Mydosh, A. Yazdani, Visualizing the formation of the Kondo lattice and the hidden order in $URu_2Si_2$. *Proc. Natl. Acad. Sci. U.S.A.* **107**, 10383–10388 (2010). Medline doi:10.1073/pnas.1005892107
16. F. Bourdarot, E. Hassinger, S. Raymond, D. Aoki, V. Taufour, L.-P. Regnault, J. Flouquet, Precise study of the resonance at $\mathbf{Q}_0$=(1,0,0) in $URu_2Si_2$. *J. Phys. Soc. Jpn.* **79**, 064719 (2010). doi:10.1143/JPSJ.79.064719
17. J. S. Hall, U. Nagel, T. Uleksin, T. Rõõm, T. Williams, G. Luke, T. Timusk, Observation of multiple-gap structure in hidden order state of $URu_2Si_2$ from optical conductivity. *Phys. Rev. B* **86**, 035132 (2012). doi:10.1103/PhysRevB.86.035132
18. W. T. Guo, Z. G. Chen, T. J. Williams, J. D. Garrett, G. M. Luke, N. L. Wang, Hybridization gap versus hidden-order gap in $URu_2Si_2$ as revealed by optical spectroscopy. *Phys. Rev. B* **85**, 195105 (2012). doi:10.1103/PhysRevB.85.195105
19. R. Okazaki, T. Shibauchi, H. J. Shi, Y. Haga, T. D. Matsuda, E. Yamamoto, Y. Onuki, H. Ikeda, Y. Matsuda, Rotational symmetry breaking in the hidden-order phase of $URu_2Si_2$. *Science* **331**, 439–442 (2011). Medline doi:10.1126/science.1197358
20. S. Tonegawa, S. Kasahara, T. Fukuda, K. Sugimoto, N. Yasuda, Y. Tsuruhara, D. Watanabe, Y. Mizukami, Y. Haga, T. D. Matsuda, E. Yamamoto, Y. Onuki, H. Ikeda, Y. Matsuda, T. Shibauchi, Direct observation of lattice symmetry breaking at the hidden-order transition in $URu_2Si_2$. *Nat. Commun.* **5**, 4188 (2014). doi:10.1038/ncomms5188
21. J. R. Jeffries, K. T. Moore, N. P. Butch, M. B. Maple, Degree of 5f electron localization in $URu_2Si_2$: Electron energy-loss spectroscopy and spin-orbit sum rule analysis. *Phys. Rev. B* **82**, 033103 (2010). doi:10.1103/PhysRevB.82.033103
22. See supporting materials on *Science* Online.
23. L. N. Ovander, *Opt. Spectrosc.* **9**, 302 (1960).
24. J. A. Koningstein, O. S. Mortensen, Experimental observation of an antisymmetric raman scattering tensor. *Nature* **217**, 445–446 (1968). doi:10.1038/217445a0
25. S. L. Cooper, M. V. Klein, M. B. Maple, M. S. Torikachvili, Magnetic excitations and phonon anomalies in $URu_2Si_2$. *Phys. Rev. B* **36**, 5743–5746 (1987). doi:10.1103/PhysRevB.36.5743
26. B. S. Shastry, B. I. Shraiman, Raman Scattering in Mott-Hubbard Systems. *Int. J. Mod. Phys. B* **5**, 365–388 (1991). doi:10.1142/S0217979291000237
27. D. V. Khveshchenko, P. B. Wiegmann, Raman scattering and anomalous current algebra in Mott insulators. *Phys. Rev. Lett.* **73**, 500–503 (1994). Medline doi:10.1103/PhysRevLett.73.500
28. H. Rho, M. V. Klein, P. C. Canfield, Polarized Raman scattering studies of crystal-field excitations in $ErNi_2B_2C$. *Phys. Rev. B* **69**, 144420 (2004). doi:10.1103/PhysRevB.69.144420
29. F. Bourdarot, B. Fåk, K. Habicht, K. Prokeš, Inflection point in the magnetic field dependence of the ordered moment of $URu_2Si_2$ observed by neutron scattering in fields up to 17 T. *Phys. Rev. Lett.* **90**, 067203 (2003). Medline

doi:10.1103/PhysRevLett.90.067203
30. C. Bareille, F. L. Boariu, H. Schwab, P. Lejay, F. Reinert, A. F. Santander-Syro, Momentum-resolved hidden-order gap reveals symmetry breaking and origin of entropy loss in $URu_2Si_2$. *Nat. Commun.* **5**, 4326 (2014). doi:10.1038/ncomms5326
31. A. R. Schmidt, M. H. Hamidian, P. Wahl, F. Meier, A. V. Balatsky, J. D. Garrett, T. J. Williams, G. M. Luke, J. C. Davis, Imaging the Fano lattice to 'hidden order' transition in $URu_2Si_2$. *Nature* **465**, 570–576 (2010). Medline doi:10.1038/nature09073
32. J. Buhot, M. A. Méasson, Y. Gallais, M. Cazayous, A. Sacuto, G. Lapertot, D. Aoki, Symmetry of the excitations in the hidden order state of $URu_2Si2$. *Phys. Rev. Lett.* **113**, 266405 (2014). Medline doi:10.1103/PhysRevLett.113.266405
33. T. D. Matsuda, D. Aoki, S. Ikeda, E. Yamamoto, Y. Haga, H. Ohkuni, R. Settai, Y. Ōnuki, Super clean sample of $URu_2Si_2$. *J. Phys. Soc. Jpn.* **77** (suppl. A), 362 (2008). doi:10.1143/JPSJS.77SA.362
34. T. D. Matsuda, E. Hassinger, D. Aoki, V. Taufour, G. Knebel, N. Tateiwa, E. Yamamoto, Y. Haga, Y. Ōnuki, Z. Fisk, J. Flouquet, Details of sample dependence and transport properties of $URu_2Si_2$. *J. Phys. Soc. Jpn.* **80**, 114710 (2011). doi:10.1143/JPSJ.80.114710
35. R. Baumbach, Z. Fisk, F. Ronning, R. Movshovich, J. D. Thompson, E. D. Bauer, High purity specimens of $URu_2Si_2$ produced by a molten metal flux technique. *Philos. Mag.* **94**, 3663–3671 (2014). doi:10.1080/14786435.2014.895876
36. G. Blumberg, R. Liu, M. Klein, W. Lee, D. Ginsberg, C. Gu, B. Veal, B. Dabrowski, Two-magnon Raman scattering in cuprate superconductors: Evolution of magnetic fluctuations with doping. *Phys. Rev. B* **49**, 13295–13298 (1994). doi:10.1103/PhysRevB.49.13295
37. P. R. Bevington, D. K. Robinson, *Data Reduction and Error Analysis for the Physical Sciences* (McGraw-Hill, New York).
38. J. Buhot *et al*., Lattice dynamics of the heavy fermion compound $URu_2Si_2$. *Phys. Rev. B* **91**, 035129 (2015). doi:10.1103/PhysRevB.91.035129
39. J. Buhot, M.-A. Méasson, Y. Gallais, M. Cazayous, A. Sacuto, G. Lapertot, D. Aoki, Raman scattering study of the lattice dynamic of $URu_2Si_2$ and sample's preparation. *J. Korean Phys. Soc.* **62**, 1427–1430 (2013). doi:10.3938/jkps.62.1427
40. P. G. Niklowitz, C. Pfleiderer, T. Keller, M. Vojta, Y. K. Huang, J. A. Mydosh, Parasitic small-moment antiferromagnetism and nonlinear coupling of hidden order and antiferromagnetism in $URu_2Si_2$ observed by Larmor diffraction. *Phys. Rev. Lett.* **104**, 106406 (2010). Medline doi:10.1103/PhysRevLett.104.106406
41. A. F. Santander-Syro, M. Klein, F. L. Boariu, A. Nuber, P. Lejay, F. Reinert, Fermi-surface instability at the 'hidden-order' transition of $URu_2Si_2$. *Nat. Phys.* **5**, 637–641 (2009). doi:10.1038/nphys1361
42. F. L. Boariu, C. Bareille, H. Schwab, A. Nuber, P. Lejay, T. Durakiewicz, F. Reinert, A. F. Santander-Syro, Momentum-resolved evolution of the Kondo lattice into "hidden order" in $URu_2Si_2$. *Phys. Rev. Lett.* **110**, 156404 (2013). Medline doi:10.1103/PhysRevLett.110.156404
43. K. Haule, G. Kotliar, Complex Landau-Ginzburg theory of the hidden order in $URu_2Si_2$. *Europhys. Lett.* **89**, 57006 (2010). doi:10.1209/0295-5075/89/57006
44. H. Kusunose, H. Harima, On the Hidden Order in $URu_2Si_2$ – Antiferro Hexadecapole Order and Its Consequences. *J. Phys. Soc. Jpn.* **80**, 084702 (2011). doi:10.1143/JPSJ.80.084702
45. M. I. Aroyo *et al*., *Bulg. Chem. Commun.* **43**, 183 (2011).
46. P. Thalmeier, T. Takimoto, Signatures of hidden-order symmetry in torque oscillations, elastic constant anomalies, and field-induced moments in $URu_2Si_2$. *Phys. Rev. B* **83**, 165110 (2011). doi:10.1103/PhysRevB.83.165110

## ACKNOWLEDGMENTS

We thank J. Buhot, P. Chandra, P. Coleman, G. Kotliar, M.-A. Méasson, D.K. Morr, L. Pascut, A. Sacuto and J. Thompson for discussions. G.B. and V.K.T. acknowledge support from the US Department of Energy, Office of Basic Energy Sciences, Division of Materials Sciences and Engineering under Award DE-SC0005463. H.-H.K. acknowledges support from the National Science Foundation under Award NSF DMR-1104884. K.H. acknowledges support by NSF DMR-1405303. W.-L. Z. acknowledges support by ICAM (NSF-IMI grant DMR-0844115). Work at Los Alamos National Laboratory was performed under the auspices of the US Department of Energy, Office of Basic Energy Sciences, Division of Materials Sciences and Engineering.

## SUPPLEMENTARY MATERIALS

www.sciencemag.org/cgi/content/full/science.1259729/DC1
Material and Methods
Supplementary Text
Figs. S1 to S4
Table S1
References (*33*–*46*)

3 March 2014; accepted 30 January 2015
Published online 12 February 2015
10.1126/science.1259729

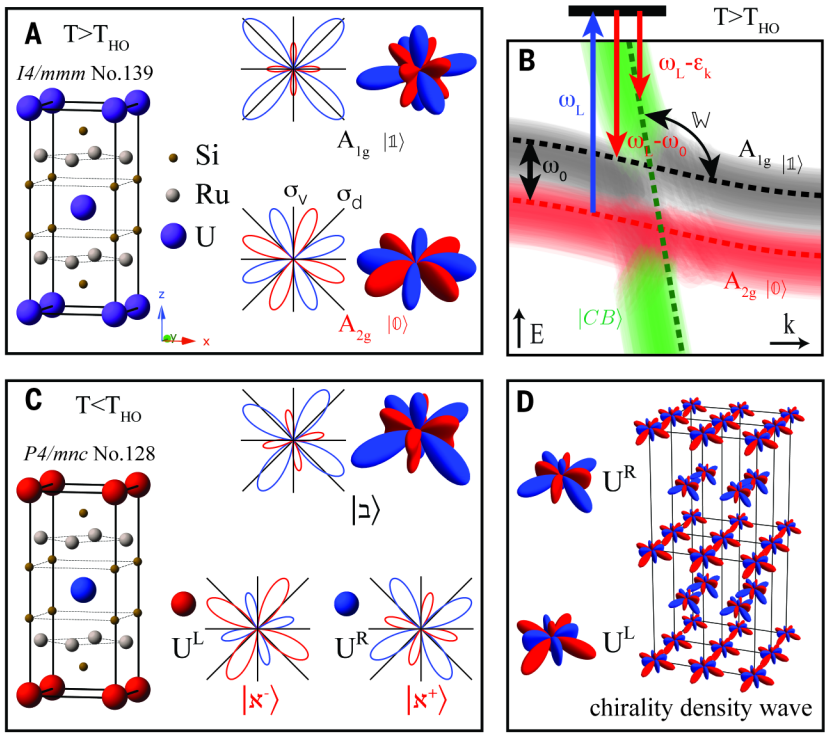


**Fig. 1. Schematics of the local symmetry of the quasi-localized states.** (**A**) The crystal structure of $URu_2Si_2$ above $T_{HO}$, belonging to the $\mathbb{D}_{4h}$ point group. Presented in 3D and *xy*-plane cut are illustrations showing the symmetry of the $A_{2g}$ state $|\mathbb{0}\rangle$ and $A_{1g}$ state $|\mathbb{1}\rangle$, where the positive (negative) amplitude is denoted by red (blue) color. The $A_{1g}$ state is symmetric with respect to the vertical ($\sigma_v$) and diagonal ($\sigma_d$) reflections, whereas the $A_{2g}$ state is antisymmetric with respect to these reflections. (**B**) Schematic of the band structure of a low energy minimal model. The green dashed line denotes the conduction band $|CB\rangle$, the red and black dashed lines denote crystal field states of the U-5*f* electrons: the ground state $|\mathbb{0}\rangle$ and the first excited state $|\mathbb{1}\rangle$ (*22*). Blue and red arrows denote the incident and scattered light in a Raman process, respectively. $\omega_L = 1.65$ eV is the incoming photon energy (energy levels not to scale), $\mathbb{W}$ is the hybridization strength between $|\mathbb{1}\rangle$ and $|CB\rangle$, $\omega_0$ and $\varepsilon_k$ are the resonance energies for $|\mathbb{0}\rangle \rightarrow |\mathbb{1}\rangle$ and $|\mathbb{0}\rangle \rightarrow |CB\rangle$ excitations, respectively. (**C**) The crystal structure of $URu_2Si_2$ in the HO phase, and illustrations showing the symmetry of the chiral states $|\aleph^+\rangle$ and $|\aleph^-\rangle$, and the excited state $|\beth\rangle$. The *left*- and *right*-handed states, denoted by red and blue atoms, respectively, are staggered in the lattice. $U^L$ and $U^R$ denotes the two non-equivalent uranium sites in the HO phase. (**D**) Schematics of the chirality density wave in the HO phase. The uranium sites $U^L$ and $U^R$ are occupied by $|\aleph^-\rangle$ and $|\aleph^+\rangle$ states, respectively.

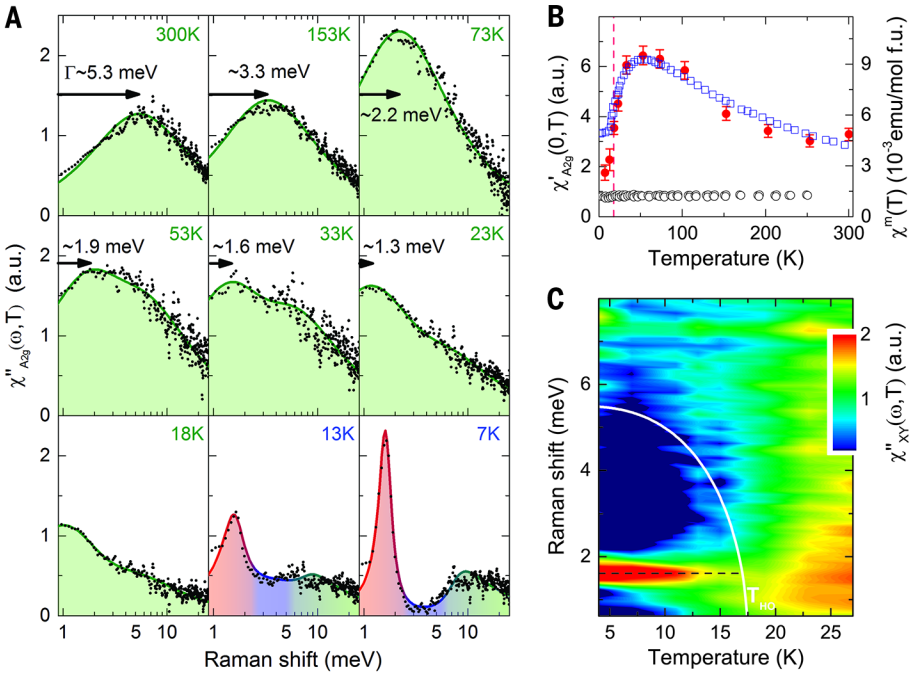


**Fig. 2. Temperature dependence of the $A_{2g}$ Raman susceptibility.** (**A**) The $A_{2g}$ Raman response function decomposed from the spectra measured in the $XY$, $X'Y'$ and $RL$ scattering geometries (*22*). The solid lines are guide to the eyes illustrating the narrowing of the Drude function (*25*): $\chi''_{A_{2g}}(\omega,T) \propto \mathrm{Im}\left[\Gamma(T) - i\omega\right]^{-1}$, where $\Gamma(T)$ is the Drude scattering rate (indicated by the arrows), which decreases on cooling. Below 70 K, the Raman response deviates from the Drude function. Below $T_{HO}$, the Raman response shows spectral weight suppression below 6 meV and the appearance of an in-gap mode at 1.6 meV (7 and 13 K). (**B**) Temperature dependence of the static Raman susceptibility in $A_{2g}$ channel: $\chi'_{A_{2g}}(0,T) = \frac{2}{\pi}\int_0^{25\mathrm{meV}} \frac{\chi''_{A_{2g}}(\omega,T)}{\omega} d\omega$ (red dots), and the static magnetic susceptibility along *c*- and *a*-axis from Ref. (*3*) are plotted as blue squares and black circles, respectively. $T_{HO}$ is marked by the dashed line. (**C**) Temperature dependence of the low frequency Raman response in the XY scattering geometry, dominantly comprised of $A_{2g}$ excitations. A gap-like suppression develops on cooling, and an in-gap mode at 1.6 meV (black dashed line) emerges below $T_{HO}$. The full-width-at-half-maximum of the mode decreases on cooling from ~0.75 meV at 13 K to ~0.3 meV at 7 K. The white line shows the temperature dependence of the BCS gap function.

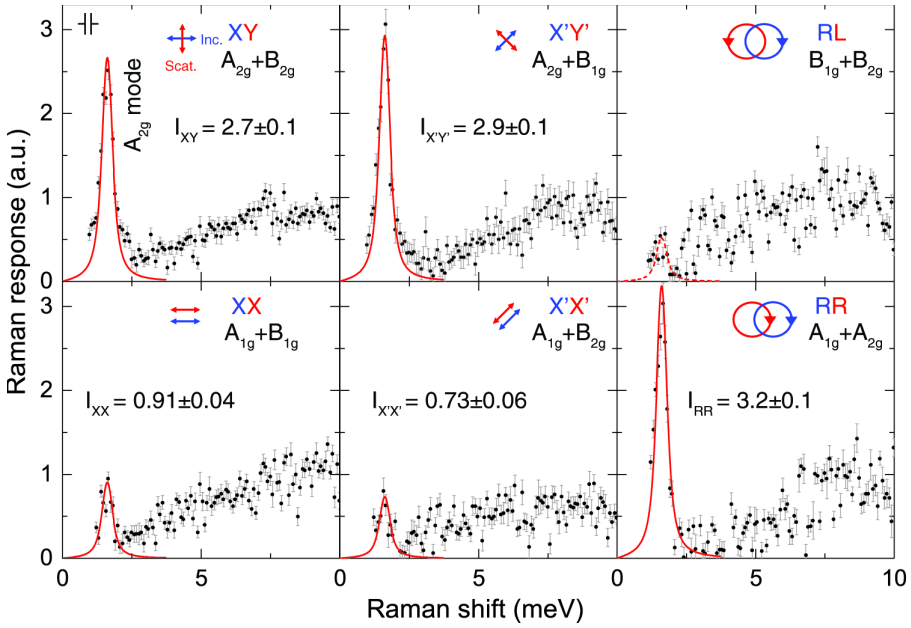


**Fig. 3. The Raman response function in six scattering geometries at 7 K.** The arrows in each panel show the linear or circular polarizations for incident (blue) and scattered (red) light. The six scattering geometries are denoted as $\mathbf{e_i e_s} = \mathrm{XX}, \mathrm{XY}, \mathrm{X'X'}, \mathrm{X'Y'}, \mathrm{RR}$ and $\mathrm{RL}$, with $\mathbf{e_i}$ being the direction vector for incident light polarization, and $\mathbf{e_s}$ being the scattered light polarization. $\mathrm{X} = [100]$, $\mathrm{Y} = [010]$ are aligned along crystallographic axes, $\mathrm{X'} = [110]$, $\mathrm{Y'} = [1\bar{1}0]$ are at $45^\circ$ to the *a*-axes, $\mathrm{R} = (\mathrm{X} + i\mathrm{Y})/\sqrt{2}$ and $\mathrm{L} = (\mathrm{X} - i\mathrm{Y})/\sqrt{2}$ are right and left circularly polarized light, respectively (*22*). The irreducible representations for each scattering geometry are shown within the $\mathbb{D}_{4h}$ point group. The data are shown in black circles, where the error bars show one standard deviation. The red solid lines are fits of the in-gap mode to a Lorentzian, and the fitted intensity using the method of maximum likelihood is noted in each panel. By decomposition, the in-gap mode intensity in each symmetry channels are: $\mathrm{I}_{\mathrm{A}_{2g}} = 2.6 \pm 0.1$, $\mathrm{I}_{\mathrm{A}_{1g}} = 0.7 \pm 0.1$, $\mathrm{I}_{\mathrm{B}_{1g}} = 0.3 \pm 0.1$, and $\mathrm{I}_{\mathrm{B}_{2g}} = 0.1 \pm 0.1$. The full width at half maximum of the in-gap mode is about 0.3 meV at 7 K (instrumental resolution of 0.17 meV is shown in the $\mathrm{XY}$ panel).